

Search for ultralight dark matter with spectroscopy of radio-frequency atomic transitions

Xue Zhang¹,¹ Abhishek Banerjee²,² Mahapan Leyser,¹ Gilad Perez²,²
Stephan Schiller³,³ Dmitry Budker^{1,4},^{1,4} and Dionysios Antypas^{1,*}

¹*Johannes Gutenberg-Universität Mainz, Helmholtz-Institut Mainz, GSI
Helmholtzzentrum für Schwerionenforschung, 55128 Mainz, Germany*

²*Department of Particle Physics and Astrophysics, Weizmann Institute of Science, Rehovot 761001, Israel*

³*Heinrich-Heine-Universität Düsseldorf, 40225 Düsseldorf, Germany*

⁴*Department of Physics, University of California, Berkeley, California 94720, USA*
(Dated: December 9, 2022)

The effects of scalar and pseudoscalar ultralight bosonic dark matter (UBDM) were searched for by comparing the frequency of a quartz oscillator to that of a hyperfine-structure transition in ^{87}Rb , and an electronic transition in ^{164}Dy . We constrain linear interactions between a scalar UBDM field and Standard-Model (SM) fields for an underlying UBDM particle mass in the range $1 \times 10^{-17} - 8.3 \times 10^{-13}$ eV and quadratic interactions between a pseudoscalar UBDM field and SM fields in the range $5 \times 10^{-18} - 4.1 \times 10^{-13}$ eV. Within regions of the respective ranges, our constraints on linear interactions significantly improve on results from previous, direct searches for oscillations in atomic parameters, while constraints on quadratic interactions surpass limits imposed by such direct searches as well as by astrophysical observations.

Introduction— Apparently, dark matter (DM) makes up the majority of matter in our Universe [1], as indicated by decades of astronomical and cosmological observations [2], and yet the nature and composition of DM remain unknown. There is a broad class of well-motivated models, where the DM constituent is a spin-0 particle with mass in the range of $m_\phi \approx 10^{-22} - 10$ eV [2, 3]. These ultralight bosonic dark matter (UBDM) particles are predicted to behave locally like a classical field, coherently oscillating at the particle’s Compton frequency $f_C = m_\phi/(2\pi)$.

The interaction between the UBDM field and the Standard-Model (SM) fields varies between different models, according to the UBDM symmetry properties such as CP (see [4] for a recent discussion). The UBDM particle could be a parity-even scalar field (dilaton), associated with spontaneous breaking of the scale-invariance symmetry (see for example [5, 6]). Alternatively, it could be a relaxion, a special kind of axion-like particle, that couples to SM matter, dominantly, via its mixing with the Higgs boson [7–10]. Interestingly, even in the celebrated case of the CP-odd QCD axion [11–13], originally proposed to explain the smallness of CP-violation in the strong force [14–21], there are quadratic-scalar interactions between the QCD-axion field and the SM ones [22]. Further exotic models dominated by a quadratically-coupled UBDM were recently described in [4].

An interaction between an ultralight scalar field and SM fields may induce violation of Einstein’s equivalence principle (EP)[23–25] and oscillations in the fundamental constants (FCs) of nature [5, 8]. Such FCs include the fine-structure constant α , electron mass m_e , and constants which determine the nuclear mass, for instance,

the QCD energy scale Λ_{QCD} and the quark masses. For a QCD-axion UBDM, oscillating nucleon electric-dipole moments are expected in case of linear coupling, [26], and, as pointed out recently [22], oscillations in nuclear parameters such as nucleon masses and nuclear g -factors are also predicted due to the presence of quadratic coupling (see also [27] for discussion on oscillating FCs due to quadratic coupling to the SM fields).

Experiments designed to check for EP violation offer a way to probe scalar UBDM [28–31]. Other works aim to detect the effects of light scalar fields by searching for oscillations in FCs. These would appear as oscillations in the length or density of solids, or in the energies of atomic or molecular levels. Various searches were proposed or completed [32–53]; see [54] for a review of experimental activities. Pseudoscalar UBDM may also introduce oscillatory effects in atomic or molecular systems [22, 27], yielding observables that are indistinguishable from these due to scalar UBDM. This enables one to probe both classes of UBDM models with the same apparatus.

Here we search for the effects of scalar UBDM in two distinct experiments, where we compare the frequency of a quartz oscillator to the frequency of either of two radio-frequency (rf) transitions: a hyperfine transition between electronic ground levels in ^{87}Rb (Experiment 1), and an electric-dipole transition between two nearly degenerate states in ^{164}Dy (Experiment 2). These searches are implemented in the UBDM particle mass range $m_\phi \approx 1 \times 10^{-17} - 8.3 \times 10^{-13}$ eV. Part of this range has thus far remained comparatively unexplored for scalar UBDM, since it is out of reach for both state-of-the-art atomic clock searches (e.g. [44, 45]) and a search with a gravitational-wave detector [39]. In addition to scalar UBDM, we search for pseudoscalar UBDM in the range $m_\phi \approx 5 \times 10^{-18} - 4.1 \times 10^{-13}$ eV employing the sensitivity of Experiment 1 to the QCD axion and improving over the results of previous laboratory searches

* dantypas@uni-mainz.de

in a part of this mass range.

UBDM detection approach — In the presence of scalar UBDM-SM interactions which are first order in the UBDM field [55], FCs such as α , m_e and Λ_{QCD} may acquire time-dependent components:

$$\alpha(t) = \alpha_0 \left[1 + d_e \frac{\phi(t)}{M_{\text{Pl}}} \right], \quad (1)$$

$$m_e(t) = m_{e,0} \left[1 + d_{m_e} \frac{\phi(t)}{M_{\text{Pl}}} \right], \quad (2)$$

$$\Lambda_{\text{QCD}}(t) = \Lambda_{\text{QCD},0} \left[1 + d_g \frac{\phi(t)}{M_{\text{Pl}}} \right]. \quad (3)$$

Here $m_{e,0}$, α_0 and $\Lambda_{\text{QCD},0}$ are the time-averaged values of the constants, $\phi(t) = \phi_0 \sin(2\pi f_{\text{C}} t)$ is the UBDM field of amplitude $\phi_0 = m_\phi^{-1} \sqrt{2\rho_{\text{DM}}}$, where $\rho_{\text{DM}} \approx 3 \cdot 10^{-6} \text{ eV}^4$ is the estimated local galactic UBDM density [2], $M_{\text{Pl}} = \sqrt{\frac{\hbar c}{8\pi G_{\text{N}}}} = 2.4 \times 10^{18} \text{ GeV}$ is the reduced Planck mass (with G_{N} being the Newtonian gravitational constant), and d_e , d_{m_e} , and d_g are the respective couplings.

If instead, UBDM is due to the pseudoscalar QCD-axion field, because of axion-pion mixing, the oscillating axion background is expected to induce a temporal dependence of the pion mass [56], and thus add an oscillating component to the nucleon masses and the nuclear g -factor [22]. In this case, the proton mass m_{p} , and the nuclear g -factor for ^{87}Rb (g_{nuc}) can be written as [22, 57]:

$$m_{\text{p}}(t) = m_{\text{p},0} \left[1 - \frac{6.6 \times 10^{-3}}{f_\phi^2} \phi(t)^2 \right], \quad (4)$$

$$g_{\text{nuc}}(t) = g_{\text{nuc},0} \left[1 + \frac{2.6 \times 10^{-3}}{f_\phi^2} \phi(t)^2 \right], \quad (5)$$

where, $m_{\text{p},0}$, $g_{\text{nuc},0}$ are the time-averaged values of the parameters, and $1/f_\phi$ is the QCD-axion coupling with the SM gluon fields, with f_ϕ being the QCD-axion decay constant.

The essence of our UBDM detection approach is to compare the frequencies of two systems (atomic vs. acoustic resonance) that depend on oscillating parameters differently. Generally, a change of a constant λ by $\delta\lambda$ may change the resonance frequency, f_i , by δf_i , which can be quantified with a sensitivity coefficient $K_i^\lambda = (\delta f_i/f_i)/(\delta\lambda/\lambda_0)$ [58]. In frequency comparison of two systems i and j , done for example by tuning one frequency close to the other, so that $f_i \approx f_j = f$, the difference $\delta f = \delta f_i - \delta f_j$ will also change with $\delta\lambda$ as long as the two oscillators exhibit different sensitivity to λ . The fractional change can be written as $\delta f/f = (K_i^\lambda - K_j^\lambda)\delta\lambda/\lambda_0$, or assuming n FCs changing:

$$\frac{\delta f}{f} = \sum_n (K_i^{\lambda_n} - K_j^{\lambda_n}) \frac{\delta\lambda_n}{\lambda_{0,n}}. \quad (6)$$

Equation (6) is applied in comparing the frequency f_{Q} of a quartz-crystal oscillator to: i) the ground-state hyperfine resonance frequency f_{HF} in ^{87}Rb (comparison 1), and ii) the frequency f_{Dy} of an rf electronic transition in ^{164}Dy (comparison 2). The relevant sensitivity coefficients are given in Table I.

The quartz frequency f_{Q} depends on α , m_e and the nuclear mass $m_{\text{N}} \propto A \cdot \Lambda_{\text{QCD}}$ [47], where A is the mass number. An atomic hyperfine frequency f_{HF} depends primarily on α , m_e and $m_{\text{p}} \propto \Lambda_{\text{QCD}}$ but with different sensitivities compared to f_{Q} . Thus, comparison 1 allows to probe oscillations of α , m_e and Λ_{QCD} within the assumption of scalar couplings. (The frequency f_{HF} depends additionally on the quark masses with sensitivity coefficients $\ll 1$ [59]; these contributions are omitted here.) Comparison 1 is one of few ways to probe oscillations of the nuclear mass [52, 53], and it extends the investigated frequency range for FC oscillations of a previous search based on a quartz/H maser comparison [47]. Applying Eq. (6) with the use of Eqs. (1–3) and the values in Table I, one obtains for the fractional frequency oscillations due to a scalar UBDM field:

$$\begin{aligned} \frac{\delta f_{\text{HF}} - \delta f_{\text{Q}}}{f} &= 2.34 \frac{\delta\alpha}{\alpha_0} + \frac{1}{2} \frac{\delta m_e}{m_{e,0}} - \frac{1}{2} \frac{\delta\Lambda_{\text{QCD}}}{\Lambda_{\text{QCD},0}} \\ &= (2.34 d_e + \frac{1}{2} d_{m_e} - \frac{1}{2} d_g) \frac{\phi(t)}{M_{\text{Pl}}}, \end{aligned} \quad (7)$$

We further consider comparison 1 via the quadratic coupling of the QCD-axion field, and make use of Eq. (4), (5) and Table I to write Eq. (6) as

$$\frac{\delta f_{\text{HF}} - \delta f_{\text{Q}}}{f} = \frac{\delta g_{\text{nuc}}}{g_{\text{nuc},0}} - \frac{1}{2} \frac{\delta m_{\text{p}}}{m_{\text{p},0}} = \frac{5.9 \times 10^{-3}}{f_\phi^2} \phi(t)^2. \quad (8)$$

We see that, due to the quadratic coupling of $\phi(t)$, oscillations of $\delta f/f$ would appear at twice the UBDM particle's Compton frequency.

TABLE I: Assumed fractional sensitivities of oscillator/transition frequencies to different FCs, relevant for scalar and pseudoscalar interactions.

	Scalar			Pseudoscalar		Ref.
	K^α	K^{m_e}	$K^{\Lambda_{\text{QCD}}}$	$K^{m_{\text{p}}}$	$K^{g_{\text{nuc}}}$	
Quartz	2	3/2	-1/2	-1/2	-	[47]
^{87}Rb	4.34	2	-1	-1	1	[59]
^{164}Dy	2.6×10^6	1	-	-	-	[60]

If no oscillations of $\delta f/f$ are detected, Eq. (7) can be used to constrain the couplings d_e , d_{m_e} , d_g for scalar UBDM, and Eq. (8) the coupling $1/f_\phi$ for QCD-axion UBDM. Note that, although $1/f_\phi$ and m_ϕ are related for the QCD axion [14–21], here we treat them as independent quantities and estimate the reach of the experiment within a more general class of models.

In comparison 2, we benefit from using an electronic transition in Dy exhibiting extreme sensitivity to changes of α . The transition is between two nearly degenerate, excited energy levels: the $4f^95d^26s$ and $4f^{10}5d6s$ levels. Primarily due to the small transition frequency f_{Dy} (754 MHz in ^{164}Dy) and significant relativistic effects, the transition has large fractional sensitivity to α changes [60–62]. It has been employed for searches of linear-in-time drift of α and α oscillations [41] on time scales from several seconds to years. Here we extend the search in the previous work [41], primarily addressing a frequency range for the FC oscillations (100 mHz-200 Hz) that was not explored in [41]. We focus on scalar UBDM and oscillations of α , and write, analogously to Eq. (7):

$$\frac{\delta f_{\text{Dy}} - \delta f_{\text{Q}}}{f} \approx 2.6 \times 10^6 \frac{\delta \alpha}{\alpha_0} = 2 \times 10^6 d_e \frac{\phi(t)}{M_{\text{PI}}}. \quad (9)$$

Since Dy sensitivity to α is vastly larger than that of quartz, the comparison 2 has practically no dependence on the quartz frequency oscillating with α .

Apparatus.— In both experiments, spectroscopy of the respective rf transitions is implemented, probing atoms with an rf field produced from a quartz oscillator. The apparatus are described in detail in the Sup. Mat.

Apparatus I implements vapor-cell-based spectroscopy of the ^{87}Rb hyperfine transition, employing the optical-microwave double-resonance technique [63]. A Rb transition is excited with a microwave field produced by mixing the output of a 100-MHz, oven-controlled, stress-compensated (SC)-cut quartz oscillator (Q_1 in Fig. 1), multiplied to 7 GHz, with the signal from a function generator. The resulting frequency is close to the hyperfine-resonance frequency of ≈ 6.83 GHz. To reduce low-frequency noise, the oscillator Q_1 is phase-locked to another oscillator (Q_2 in Fig. 1), that exhibits higher long-term frequency stability compared to Q_1 . The oscillator Q_2 is also oven-controlled and constructed around a SC-cut, quartz crystal. The phase-locked loop has a measured bandwidth of ≈ 3 Hz. Thus, for $f_C \leq 3$ Hz the dependence on the oscillating parameters (α , m_e and m_N) is determined by Q_2 , and for $f_C > 3$ Hz by Q_1 . The same dependence on the FCs is assumed for both.

Experiment 2 utilizes an atomic beam setup for spectroscopy of the Dy rf transition (see [64] and references therein). The atoms are prepared in the metastable state $4f^95d^26s$ (labeled ‘B’ in Fig. 1) via a two-step laser excitation and subsequent decay. The signal from a signal generator at ≈ 754 MHz is used to produce an electric field that induces transitions to the $4f^{10}5d6s$ state (state ‘A’), whose subsequent decay is monitored via fluorescence as a means to observe the B \rightarrow A transition, with an observed linewidth of ≈ 50 kHz. The time base for the generator is provided by an internal oven-controlled, SC-cut, quartz oscillator.

Frequency-modulation spectroscopy [63] is implemented in both experiments, to improve detection sensitivity of the atomic excitations. For this, the respective rf drive is modulated in frequency and phase-sensitive

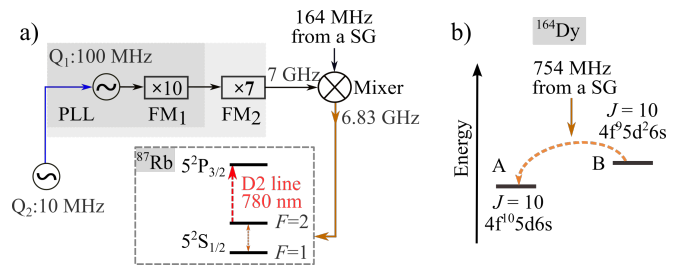


FIG. 1: a) Schematic of the setup to produce the rf signal probing the ^{87}Rb hyperfine transition at 6.83 GHz. b) The electric-dipole rf transition between the excited ^{164}Dy levels ‘B’ and ‘A’, both having the same angular momentum J .

Abbreviations: PLL: phase-locked loop; FM: frequency multipliers; SG: signal generator.

detection of the spectroscopy signal is done.

Data acquisition and analysis— In the two experiments, the spectroscopy signal was repetitively acquired for several values of the rf-modulation frequency. In apparatus I, we found that the experimental parameters providing optimal sensitivity are different for different ranges of the frequency f_C (see Sup. Mat.). Thus, in the low-frequency run, we recorded many 4-h-long time series for a total of 600 h, with a sampling rate of 41.7 Sa/s; while in the high-frequency run, we acquired a sequence of 10-min-long time series, for a total of 144 h, sampling the signal at 406.5 Sa/s. Data taking for Experiment 2 was a total of 12 h, with the spectroscopy signal sampled at 406.5 Sa/s and recorded in three successive, 4-h-long time series.

From the recorded time series, power spectra were computed and averaged. The corresponding amplitude spectra were investigated for possible signatures of oscillations that would appear as amplitudes in frequency bins of the spectra, that are greater than a threshold for detection. This threshold is determined by the random noise in the vicinity of the bins, and set to a 95% confidence level, accounting for the look-elsewhere effect [65] (see Sup. Mat.). We checked this set threshold by injecting artificial signals to the recorded time series, and looking at the size of the respective amplitudes in the computed spectra (see Sup. Mat.).

A total of ten peaks were observed to exceed the threshold for detection in the low-frequency run of Experiment 1 and 231 peaks were seen in the high-frequency run. In Experiment 2, 983 peaks were observed. All these spurious signals were checked via: i) intercomparison of the averaged amplitude spectra acquired with different modulation frequencies; ii) cross-checks between the spectra acquired for the low- and high-frequency range runs (relevant in Experiment 1); iii) comparison of primary data sets against sets from auxiliary runs with an alternative signal generator (see Fig. 1). As an actual UBDM signal should persist in all these tests, eventually all spurious peaks were excluded from being UBDM candidates, allowing us to constrain the spectra of the frac-

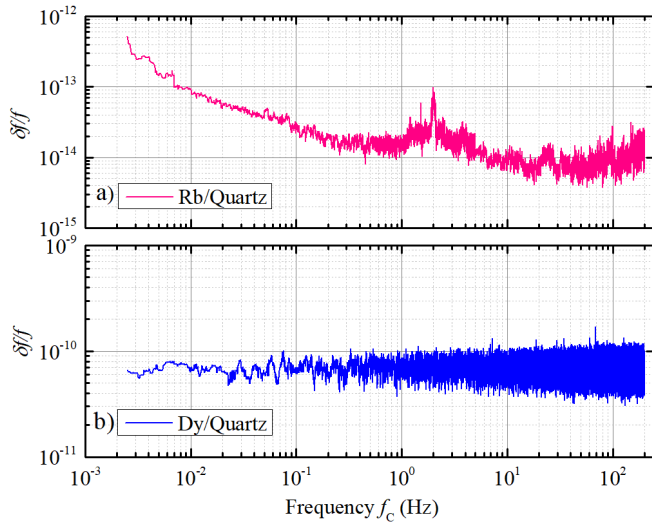


FIG. 2: Exclusion limits on fractional frequency oscillations $\delta f/f$ at 95% C.L. a) Experiment 1. The spectrum is produced by merging the spectra from the low- and high-frequency runs at 5 Hz, i.e. the frequency where the respective FC detection sensitivities become equal. We do not provide limits in the frequency windows 50 ± 0.25 Hz and 100 ± 0.25 Hz. b) Experiment 2. The spectrum exhibits no pronounced dependence on frequency, as the dominant noise source is shot noise in the detection of Dy transitions in the atomic beam.

tional frequency oscillations $\delta f/f$, as shown in Fig. (2) [66].

Constraints on UBDM couplings—We use the constraints on $\delta f/f$ (Fig. 2) and Eq. (6), (7),(9) to bound the UBDM couplings to α , m_e and Λ_{QCD} (Fig. 3). To do this, we assume that the respective coupling dominates the UBDM-SM interaction. In addition, we consider the stochastic nature of the UBDM field [67] and apply a correction to the bounds to account for reduction in UBDM detection sensitivity that becomes appreciable at oscillation frequencies $f_C < Q/T$ [68], where $Q \approx 1.1 \times 10^6$ is the Q-factor of the UBDM field within the standard galactic UBDM halo scenario [69], and T is the total measurement time; $T = 864$ h and 12 h for experiments I and II, respectively. Applying the analysis method of [70] we find that the bounds from experiments I and II become weaker by a factor of ≈ 4.4 below ≈ 1 Hz and ≈ 50 Hz, respectively [71].

The bounds on d_e , d_{m_e} and d_g from the Rb/quartz comparison improve on previous results by as many as $\times 100$ times in the range 1–200 Hz. Within the whole range investigated (2.5 mHz–200 Hz), a variety of experiments directly probe for oscillations of α and m_e , as seen in Fig. 3a and Fig. 3b. Few experiments however, probe a hyperfine resonance (as we do in this work), and are sensitive to oscillations of the strong force (Fig. 3c).

A more stringent bound on d_e is provided by the Dy experiment. The limit $\delta f/f \approx 8 \times 10^{-11}$ translates to a limit $\delta\alpha/\alpha \approx 3 \times 10^{-17}$ and a bound on d_e that improves

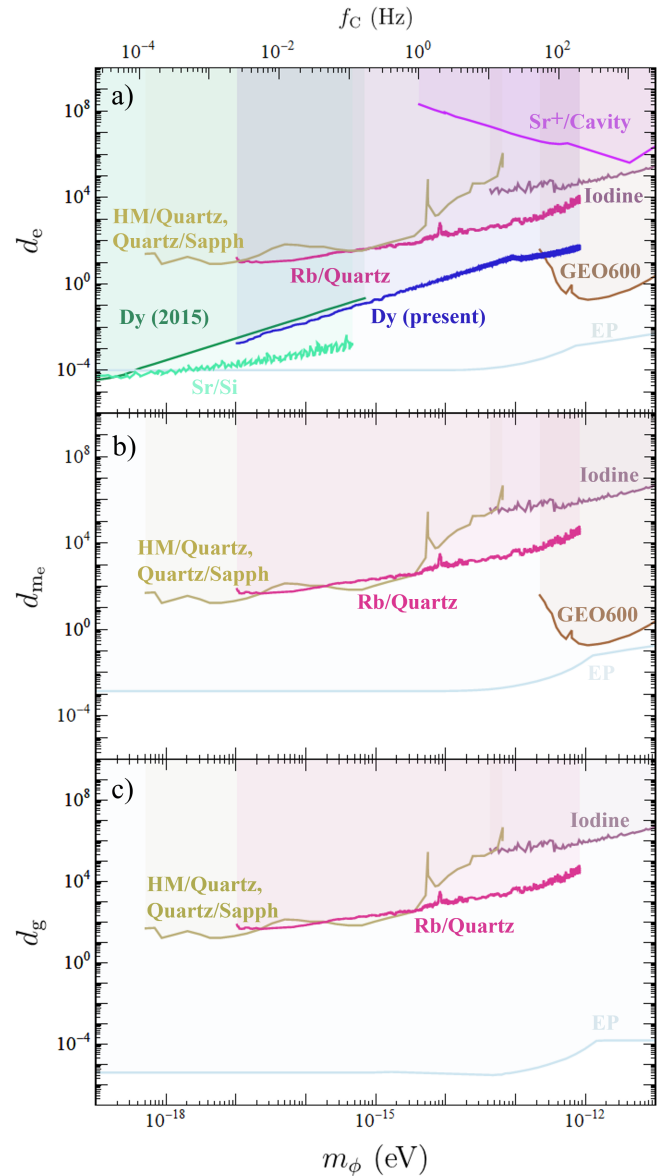


FIG. 3: Constraints on the UBDM couplings to α , m_e , and Λ_{QCD} from the present work (Rb/Quartz and Dy/Quartz), shown at the 95% C.L., alongside constraints from other experiments. Dy (2015):[41], Sr/Si: [45], Sr^+ /cavity: [46], Iodine:[53], GEO600: [39], Hydrogen Maser (HM)/Quartz-Quartz/Sapphire: [47], EP:[72–74]. The limits from [47] are plotted considering the respective parameters independently, and multiplying by a factor $\times 4.4$ to account for stochasticity of UBDM in that work, as it was done for the Rb/Quartz and Dy/Quartz data (see text).

on previous results by as many as three orders of magnitude. Having UBDM detection capability up to the frequency of the observed transition linewidth (≈ 50 kHz) the Experiment 2 is used to explore a region between the upper-frequency end in state-of-the-art atomic clock searches (e.g. [45]) and the low-frequency end of the GEO600 search [39].

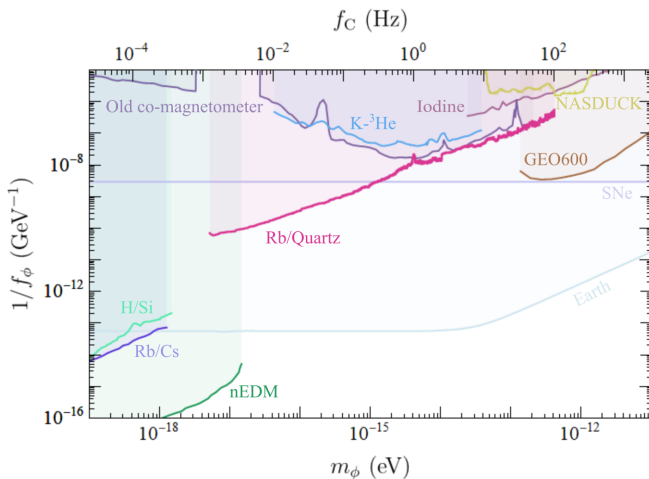


FIG. 4: Constraints on the QCD axion-gluon coupling. Rb/Cs [42], H/Si [45], nEDM [75], Iodine [53], GEO 600 [39], SNe [76], Co-magnetometer[77], NASDUCK [78], $K\text{-}^3\text{He}$ [79], Earth [80].

The assumption of pseudoscalar UBDM allows one to interpret the $\delta f/f$ limits from Experiment 1 as limits on the QCD axion-gluon coupling $1/f_\phi$ (Fig. 4) via Eq. (8). Here as well a correction is made to account for the stochasticity of UBDM; it amounts to a calculated degradation of the limit of Fig. (2) by a factor of ≈ 2.5 in the sub-Hz region. Our constraints on $1/f_\phi$ (Fig. 2) improve on those from tabletop experiments probing the effects of an axion coupling via atomic magnetometry [77, 78]. They also surpass astrophysical limits [76] in the frequency range below 200 mHz.

Conclusions and outlook — Our bounds on scalar and pseudoscalar UBDM interactions represent significant improvement over previous work in part of the explored mass range. While the limits on scalar couplings to the α , m_e and d_g from EP-violation searches are more stringent, direct searches for oscillations in these constants offer important cross-checks. In addition, as discussed in [4, 81], if the scalar UBDM has some non generic coupling to the SM, then bounds from the EP-violation/fifth-force experiments may be suppressed by a factor $\mathcal{O}(10^3)$ and may become comparable to that of FC-oscillation searches [49].

The recent work [22] pointing to oscillatory effects in nuclear parameters in the presence of the QCD axion, extends the physics reach of apparatus used thus far to check for FC oscillations. As we show here, this opens a way to probe pseudoscalar UBDM with sensitivity that is, in a certain mass range, far greater than that in setups designed to search for previously considered pseudoscalar-field observables.

This possibility motivates further apparatus improvements, for example, in probing the hyperfine resonance. The present Rb/quartz frequency comparison is at the $10^{-12}/\sqrt{\tau}$ level in the short-term (measurement time $\tau < 10$ s); this is ≈ 10 times lower than that reported for a vapor-cell-based Rb clock [82]. Long-term stability

can be improved by optimization of the parameters of the Rb-vapor-cell setup [82]. Because the stability of a quartz oscillator degrades at such long time scales, it would be necessary to replace it with a microwave signal derived from an optical atomic clock or an optical cavity [45]. Together with a long data-taking campaign, such improvements could extend the reach of an experiment by orders of magnitude, and probe for the QCD-axion further beyond the level allowed by atomic magnetometry and astrophysical observations.

We thank W. Ji for discussions and N.L.Figueroa, D. Kanta, U. Rosowski and M. Hansen for help with the project. This work was supported by the European Research Council (ERC) under the European Union Horizon 2020 research and innovation program (project Yb-FUN, grant agreement No 947696) and by the DFG Project ID 390831469: EXC 2118 (PRISMA+ Cluster of Excellence). The work of AB is supported by the Azrieli foundation.

- [1] R. L. Workman and Others (Particle Data Group), PTEP **2022**, 083C01 (2022).
- [2] D. F. Jackson Kimball and K. van Bibber, eds., *The Search for Ultralight Bosonic Dark Matter* (Springer, New York, 2023).
- [3] M. S. Safronova, D. Budker, D. DeMille, D. F. J. Kimball, A. Derevianko, and C. W. Clark, Rev. Mod. Phys. **90**, 025008 (2018).
- [4] A. Banerjee, G. Perez, M. Safronova, I. Savoray, and A. Shalit, (2022), arXiv:2211.05174 [hep-ph].
- [5] A. Arvanitaki, J. Huang, and K. Van Tilburg, Phys. Rev. D **91**, 015015 (2015).
- [6] W. Graham, P. G. Irastorza, I. K. Lamoreaux, S. A. Lindner, and A. Van Bibber, K, Annu. Rev. Nucl. Part. Sci. **65**, 485 (2015).
- [7] P. W. Graham, D. E. Kaplan, and S. Rajendran, Phys. Rev. Lett. **115**, 221801 (2015).
- [8] A. Banerjee, H. Kim, and G. Perez, Phys. Rev. D **100**, 115026 (2019).
- [9] T. Flacke, C. Frugiuele, E. Fuchs, R. S. Gupta, and G. Perez, J. High Energy Phys. **2017**, 50 (2017).
- [10] A. Banerjee, H. Kim, O. Matsedonskyi, G. Perez, and M. S. Safronova, JHEP **07**, 153 (2020), arXiv:2004.02899 [hep-ph].
- [11] J. Preskill, M. B. Wise, and F. Wilczek, Phys. Lett. B **120**, 127 (1983).
- [12] L. F. Abbott and P. Sikivie, Phys. Lett. B **120**, 133 (1983).
- [13] M. Dine and W. Fischler, Phys. Lett. B **120**, 137 (1983).
- [14] R. D. Peccei and H. R. Quinn, Phys. Rev. D **16**, 1791 (1977).
- [15] R. D. Peccei and H. R. Quinn, Phys. Rev. Lett. **38**, 1440 (1977).
- [16] S. Weinberg, Phys. Rev. Lett. **40**, 223 (1978).
- [17] F. Wilczek, Phys. Rev. Lett. **40**, 279 (1978).
- [18] J. E. Kim, Phys. Rev. Lett. **43**, 103 (1979).
- [19] M. A. Shifman, A. I. Vainshtein, and V. I. Zakharov, Nucl. Phys. B **166**, 493 (1980).
- [20] A. R. Zhitnitsky, Sov. J. Nucl. Phys. **31**, 260 (1980).
- [21] M. Dine, W. Fischler, and M. Srednicki, Phys. Lett. B **104**, 199 (1981).
- [22] H. Kim and G. Perez, (2022), arXiv:2205.12988 [hep-ph].
- [23] T. Damour and J. F. Donoghue, Phys. Rev. D **82**, 084033 (2010), arXiv:1007.2792 [gr-qc].
- [24] T. Damour and J. F. Donoghue, Phys. Rev. D **82**, 084033 (2010).
- [25] A. Hees, O. Minazzoli, E. Savalle, Y. V. Stadnik, and P. Wolf, Phys. Rev. D **98**, 064051 (2018).
- [26] P. W. Graham and S. Rajendran, Phys. Rev. D **88**, 035023 (2013), arXiv:1306.6088 [hep-ph].
- [27] Y. V. Stadnik and V. V. Flambaum, Phys. Rev. Lett. **115**, 201301 (2015).
- [28] G. L. Smith, C. D. Hoyle, J. H. Gundlach, E. G. Adelberger, B. R. Heckel, and H. E. Swanson, Phys. Rev. D **61**, 022001 (1999).
- [29] S. Schlamminger, K.-Y. Choi, T. A. Wagner, J. H. Gundlach, and E. G. Adelberger, Phys. Rev. Lett. **100**, 041101 (2008).
- [30] P. Touboul *et al.*, Phys. Rev. Lett. **119**, 231101 (2017).
- [31] J. Bergé, P. Brax, G. Métris, M. Pernot-Borrás, P. Touboul, and J.-P. Uzan, Phys. Rev. Lett. **120**, 141101 (2018).
- [32] A. Arvanitaki, S. Dimopoulos, and K. Van Tilburg, Phys. Rev. Lett. **116**, 031102 (2016).
- [33] J. Manley, D. J. Wilson, R. Stump, D. Grin, and S. Singh, Phys. Rev. Lett. **124**, 151301 (2020).
- [34] A. A. Geraci, C. Bradley, D. Gao, J. Weinstein, and A. Derevianko, Phys. Rev. Lett. **123**, 031304 (2019).
- [35] Y. V. Stadnik and V. V. Flambaum, Phys. Rev. Lett. **114**, 161301 (2015).
- [36] Y. V. Stadnik and V. V. Flambaum, Phys. Rev. A **93**, 063630 (2016).
- [37] H. Grote and Y. V. Stadnik, Phys. Rev. Research **1**, 033187 (2019).
- [38] E. Savalle, A. Hees, F. Frank, E. Cantin, P.-E. Pottie, B. M. Roberts, L. Cros, B. T. McAllister, and P. Wolf, Phys. Rev. Lett. **126**, 051301 (2021).
- [39] S. M. Vermeulen *et al.*, Nature **600**, 424 (2021).
- [40] L. Aiello, J. W. Richardson, S. M. Vermeulen, H. Grote, C. Hogan, O. Kwon, and C. Stoughton, Phys. Rev. Lett. **128**, 121101 (2022).
- [41] K. Van Tilburg, N. Leefler, L. Bougas, and D. Budker, Phys. Rev. Lett. **115**, 011802 (2015).
- [42] A. Hees, J. Guéna, M. Abgrall, S. Bize, and P. Wolf, Phys. Rev. Lett. **117**, 061301 (2016).
- [43] P. Wcislo *et al.*, Sci. Adv. **4** (2018), 10.1126/sciadv.aau4869.
- [44] K. Belay *et al.*, Nature **591**, 564 (2021).
- [45] C. J. Kennedy, E. Oelker, J. M. Robinson, T. Bothwell, D. Kedar, W. R. Milner, G. E. Marti, A. Derevianko, and J. Ye, Phys. Rev. Lett. **125**, 201302 (2020).
- [46] S. Aharony, N. Akerman, R. Ozeri, G. Perez, I. Savoray, and R. Shaniv, Phys. Rev. D **103**, 075017 (2021).
- [47] W. M. Campbell, B. T. McAllister, M. Goryachev, E. N. Ivanov, and M. E. Tobar, Phys. Rev. Lett. **126**, 071301 (2021).
- [48] D. Antypas, O. Tretiak, A. Garcon, R. Ozeri, G. Perez, and D. Budker, Phys. Rev. Lett. **123**, 141102 (2019).
- [49] O. Tretiak, X. Zhang, N. Figueroa, D. Antypas, A. Brogna, A. Banerjee, G. Perez, and D. Budker, Phys. Rev. Lett. **129**, 031301 (2022).
- [50] V. V. Flambaum, A. J. Mansour, I. B. Samsonov, and C. Weitenberg, arXiv:2210.08778 [hep-ph] (2022), <https://doi.org/10.48550/arXiv.2210.08778>.
- [51] D. Hanneke, B. Kuzhan, and A. Lunstad, Quantum Sci. Technol. **6**, 014005 (2020).
- [52] D. Antypas, O. Tretiak, K. Zhang, A. Garcon, G. Perez, M. G. Kozlov, S. Schiller, and D. Budker, Quantum Sci. Technol. **6**, 034001 (2021).
- [53] R. Oswald *et al.*, Phys. Rev. Lett. **129**, 031302 (2022).
- [54] D. Antypas *et al.*, arXiv:2203.14915 (2022).
- [55] See [4, 25] for phenomenology of second-order couplings.
- [56] L. Ubaldi, Phys. Rev. D **81**, 025011 (2010), arXiv:0811.1599 [hep-ph].
- [57] V. V. Flambaum and A. F. Tedesco, Phys. Rev. C **73**, 055501 (2006), arXiv:nucl-th/0601050.
- [58] M. G. Kozlov and D. Budker, Ann. Phys. **531**, 1800254 (2019).
- [59] V. V. Flambaum, D. B. Leinweber, A. W. Thomas, and R. D. Young, Phys. Rev. D **69**, 115006 (2004).
- [60] V. A. Dzuba, V. V. Flambaum, and M. V. Marchenko, Phys. Rev. A **68**, 022506 (2003).

- [61] V. A. Dzuba, V. V. Flambaum, and J. K. Webb, Phys. Rev. A **59**, 230 (1999).
- [62] V. A. Dzuba and V. V. Flambaum, Phys. Rev. A **77**, 012515 (2008).
- [63] W. Demtröder, *Laser Spectroscopy*, 5th ed., Vol. 2 (Springer, Berlin-Heidelberg, 2015).
- [64] N. Leefler, C. Weber, A. Cingoz, J. Torgerson, and D. Budker, Phys. Rev. Lett. **111**, 060801 (2013).
- [65] J. D. Scargle, Astrophys. J. **263**, 835 (1982).
- [66] It is challenging to reliably compute a threshold for detection of oscillation in the $\delta f/f$ spectra for $f_C < 1$ mHz (see Sup. Mat.). Here we provide constraints for $f_C \geq 2.5$ mHz.
- [67] G. P. Centers *et al.*, Nat. Commun. **12** (2021), 10.1038/s41467-021-27632-7.
- [68] To within a factor of 2π [69].
- [69] A. V. Gramolin, A. Wickenbrock, D. Aybas, H. Bekker, D. Budker, G. P. Centers, N. L. Figueroa, D. F. J. Kimball, and A. O. Sushkov, Phys. Rev. D **105**, 035029 (2022).
- [70] B. E. J. Pelssers, *Enhancing Direct Searches for Dark Matter*, Ph.D. thesis, Stockholm University, Sweden (2022).
- [71] This ≈ 4.4 correction factor may be conservative, compared to the factor ≈ 3 of [67].
- [72] P. Touboul *et al.*, Phys. Rev. Lett. **119**, 231101 (2017), arXiv:1712.01176 [astro-ph.IM].
- [73] T. A. Wagner, S. Schlamminger, J. H. Gundlach, and E. G. Adelberger, Class. Quant. Grav. **29**, 184002 (2012).
- [74] G. L. Smith, C. D. Hoyle, J. H. Gundlach, E. G. Adelberger, B. R. Heckel, and H. E. Swanson, Phys. Rev. D **61**, 022001 (2000).
- [75] C. Abel *et al.*, Phys. Rev. X **7**, 041034 (2017), arXiv:1708.06367 [hep-ph].
- [76] G. G. Raffelt, Lect. Notes Phys. **741**, 51 (2008), arXiv:hep-ph/0611350.
- [77] I. M. Bloch, Y. Hochberg, E. Kuflik, and T. Volansky, JHEP **01**, 167 (2020), arXiv:1907.03767 [hep-ph].
- [78] I. M. Bloch, G. Ronen, R. Shaham, O. Katz, T. Volansky, and O. Katz (NASDUCK), Sci. Adv. **8**, abl8919 (2022), arXiv:2105.04603 [hep-ph].
- [79] J. Y. Lee, M. Lisanti, W. A. Terrano, and M. Romalis, arXiv:2209.03289 [hep-ph] (2022), <https://doi.org/10.48550/arXiv.2209.03289>.
- [80] A. Hook and J. Huang, JHEP **06**, 036 (2018), arXiv:1708.08464 [hep-ph].
- [81] R. Oswald *et al.*, Phys. Rev. Lett. **129**, 031302 (2022), arXiv:2111.06883 [hep-ph].
- [82] T. Bandi, C. Affolderbach, C. Stefanucci, F. Merli, A. K. Skrivervik, and G. Mileti, IEEE Trans. Ultrason. Ferroelectr. Freq. Control **61**, 1769 (2014).
- [83] T. Bandi, C. Affolderbach, and G. Mileti, J. Appl. Phys. **111**, 124906 (2012).
- [84] A. T. Nguyen, G. D. Chern, D. Budker, and M. Zolotarev, Phys. Rev. A **63**, 013406 (2000).
- [85] A. Cingoz, Ph.D. thesis, University of California, Berkeley (2019).
- [86] D. Budker, D. DeMille, E. D. Commins, and M. S. Zolotarev, Phys. Rev. A **50**, 132 (1994).
- [87] P. Di Vecchia and G. Veneziano, Nucl. Phys. B **171**, 253 (1980).
- [88] C. Vafa and E. Witten, Phys. Rev. Lett. **53**, 535 (1984).
- [89] R. L. Workman (Particle Data Group), PTEP **2022**, 083C01 (2022).

SUPPLEMENTAL MATERIAL

A. Apparatus

Experiment 1 — A schematic of the Rb/quartz setup is shown in Fig. 5 a). The optical-microwave double resonance technique is applied to Rb vapor to look for the effects of ultralight bosonic dark matter (UBDM). A cylindrical cell (25 mm long, with a 25 mm diameter) containing natural-abundance Rb-metal vapor and buffer gasses (14 mbar argon and 10 mbar nitrogen) is placed in a cylindrical plastic tube that holds two wire loops which provide rf magnetic field to the atoms. This assembly lays inside a solenoid that provides a static magnetic field in the range 0.5-1 μ T, to resolve the Zeeman sublevels of the ^{87}Rb ground hyperfine levels. A pair of heater tapes are wrapped around the solenoid to heat the Rb vapor in the range 55-65 $^\circ\text{C}$. The whole assembly is placed inside a single-layer magnetic shield.

Light from a diode laser is used to drive the ^{87}Rb D2 transition at 780 nm. In order to enhance the sensitivity of the apparatus, the laser frequency noise is actively reduced by stabilizing the laser frequency to a resonance of a Fabry-Pérot cavity. The cavity is in turn stabilized to the reading of a wavemeter (High Finesse WS8-2), so that the the long-term drift of the laser frequency is suppressed and the laser frequency remains stabilized to a point where the signal from the hyperfine resonance is optimal. Another setup, allowing Doppler-free spectroscopy of the D2 line is used as an auxiliary frequency reference.

The 780 nm beam entering the vapor cell has a power of ≈ 0.2 mW and ≈ 15 mm diameter. The power of the beam is stabilized with an electro-optic amplitude modulator and a proportional-integral-derivative controller (not shown in the schematic).

The primary quartz oscillator in the setup (Q_1 in Fig. 5a) is a 100-MHz unit based on an oven-controlled, SC-cut crystal. The oscillator is integrated in a device (NEL Frequency Controls O-CEGM-017DWEP-R-1 GHz) that incorporates an analog multiplier to produce a 1-GHz output. The device is housed in a multiplier unit (NEL Frequency Controls N-DCN-SS702-000IR-7.00 GHz) that brings the signal to 7 GHz with use of analog multipliers. As mentioned in the main text, to improve low-frequency noise performance, the 100-MHz oscillator is phase-locked with a bandwidth of ≈ 3 Hz to another, more stable, 10-MHz oscillator (Q_2 in Fig. 5a), constructed around an oven-controlled, SC-cut quartz (NEL Frequency Controls O-CE1-0S19HR-N-E-N-R 10.000 MHz). The 7-GHz signal is mixed with use of a frequency mixer (Mini-Circuits ZX06-U742MH-S+) with a ≈ 164 -MHz signal from a signal generator (SRS SG386) to produce a field at 6.83 GHz that drives the ^{87}Rb hyperfine transition. The generator's internal time base is another SC-cut quartz oscillator. The 164-MHz signal of the generator is frequency-modulated, as further explained below.

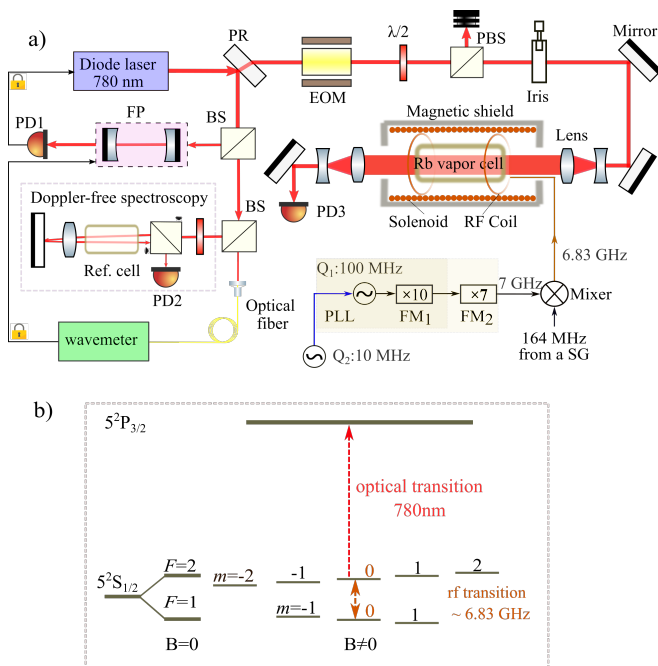


FIG. 5: a) Experimental setup for Experiment 1. PR: partial reflector; EOM: electro-optic modulator; $\lambda/2$: half-wave plate; (P)BS: (polarizing) beam splitter; FP: Fabry-Pérot optical cavity; PD: photodetector. PLL: phase-locked loop; FM: frequency multipliers. Q1, Q2: quartz oscillators. b) Optical-microwave double resonance for ^{87}Rb . The red dashed line indicates optical pumping and the orange dashed line shows hyperfine transition between the clock state.

The principle of the double-resonance technique is illustrated in Fig. 5b [83]. Our 780-nm laser is tuned in frequency to excite the D2 transition from the $5^2S_{1/2} |F=2\rangle$ ground level. Atoms are thus pumped to the other ground level, the $5^2S_{1/2} |F=1\rangle$ level, resulting in reduction of population of the $|F=2\rangle$ level. An rf field at 6.83 GHz drives the hyperfine $|F=1, m=0\rangle \rightarrow |F=2, m=0\rangle$ clock transition between the two ground states, leading to an increase of the population of the $|F=2, m=0\rangle$ state, and resulting in decreased transmission of the 780 nm light through the atomic sample. This transmission signal is a probe of the hyperfine resonance. The resulting spectrum, produced as the frequency of the rf field is swept around the hyperfine resonance, is shown in Fig. 7a). Modulation of the rf-field frequency and demodulation with a lock-in amplifier provides a dispersion-shaped resonance signal, that is used as a frequency discriminator in the search for oscillating UBDM effects. The slope of the linear part of the dispersion-shape resonance is measured and used to calibrate the response, i.e. to convert the computed amplitude spectra described in the main text to $\delta f/f$ spectra.

Experiment 2 — A schematic of the Dy spectroscopy setup is shown in Fig. 6a. A thermal beam of Dy atoms,

effusing from an oven heated to 1400 K, is collimated with a pair of slits, and optically pumped via two-step excitation using light at 833 nm and 669 nm produced with diode lasers. This excitation is done with diverging laser beams in order to excite all atoms in the atomic beam [84]. The excitation, shown in Fig. 6b, populates the state $4f^{10}5d6s |J=9\rangle$ that spontaneously decays with a 30% branching ratio into state B [84]. An ac electric field at 754 MHz induces an electric-dipole transition between states B and A. The ac field is applied in the so-called interaction region, with parallel grids of 50- μm -thick Be-Cu wires constituting electric field “plates”. (A detailed description of the rf interaction region is given in [85].) Atoms in state A (with lifetime of $\approx 8 \mu\text{s}$ [64, 86]) exhibit cascade decay to the ground state $4f^{10}6s^2 |J=8\rangle$ emitting fluorescence at 564 nm collected with a photomultiplier. This fluorescence is a probe of the rf resonance. The 754-MHz signal driving the Dy transition is produced with the same signal generator used in Experiment 1. As in Experiment 1, frequency modulation on the generator’s output is done for phase-sensitive detection of the fluorescence signal Fig. 7b, using a lock-in amplifier. The demodulated signal, as in Experiment 1, serves as a frequency discriminator in the search for FC oscillations, whose linear part (as in Experiment 1) is used to calibrate the apparatus response.

B. Data acquisition methods

Experiment 1 — As mentioned in the main text, we find that experimental conditions providing optimal detection sensitivity are different for low and high frequencies. Therefore, we carry out separate low- and high-frequency data-taking runs.

The low-frequency run probes the range 2.5 mHz-5 Hz. The sensitivity is optimal for a vapor-cell temperature $\approx 55^\circ\text{C}$, an optical intensity $\approx 1.12 \mu\text{W}/\text{mm}^2$, and an rf-drive power corresponding to a hyperfine-resonance linewidth of ≈ 550 Hz.

A commercial 16-bit digitizer (PicoScope 5244D) is used for data acquisition. Data taking in the low-frequency run consists of recording the demodulated hyperfine-resonance signal in 4-h-long time series for a total of 600 h, at a sampling rate of $\approx 41.7 \text{ Sa/s}$. We alternate acquisition with the modulation frequency set one of two distinct values. This allows for intercomparison of spurious signals acquired in the respective spectra, and elimination of such signals as UBDM candidates. The 600-h recorded data involves 150 time series, of which 75 are obtained with modulation frequency of 177 Hz and another 75 with 144 Hz.

In the high-frequency run, we focus on the 5–200 Hz frequency range. Here the rf-drive power yielding optimal sensitivity results in a hyperfine-transition linewidth of ≈ 1 kHz; the Rb-cell temperature is $\approx 65^\circ\text{C}$, and the optical intensity $\approx 1.12 \mu\text{W}/\text{mm}^2$. The digitizer is set to ac-couple the signal (with cut-off at 1.5 Hz) to eliminate

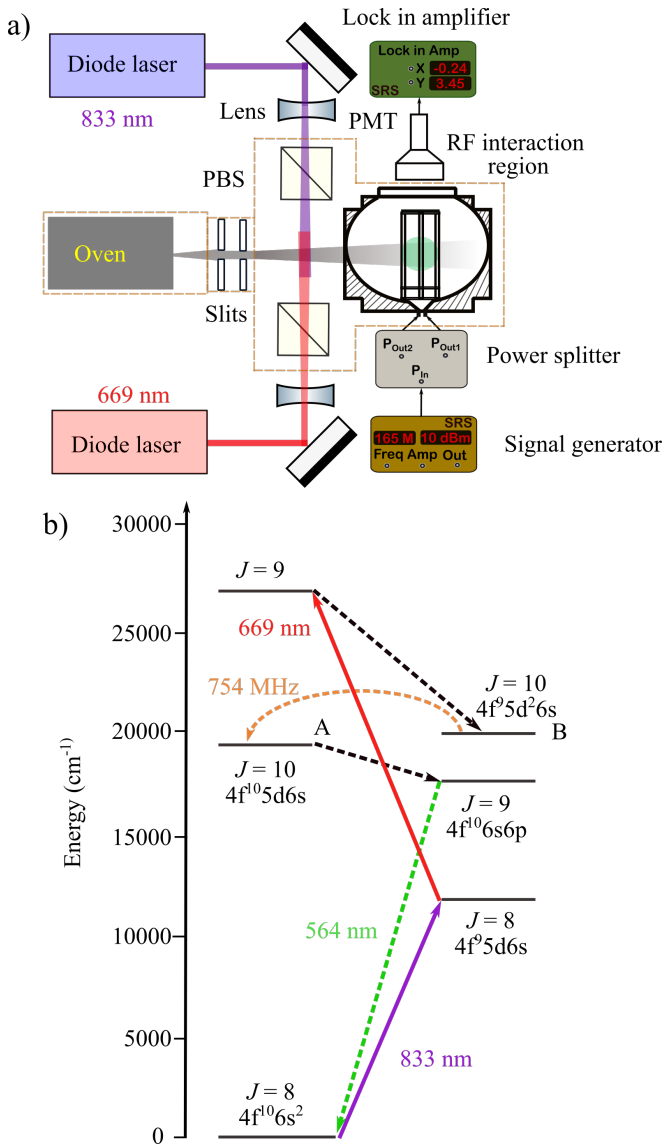


FIG. 6: a) Apparatus schematic of Experiment 2. Components within orange dashed boundaries are in vacuum. b) Partial energy level diagram of Dy. The employed rf electric-dipole transition is between the nearly degenerate states, labeled ‘A’ and ‘B’. Atoms are prepared in state B via two-step laser excitation followed by a spontaneous decay. Cascade decay from state A to the ground state yields fluorescence at 564 nm (green dashed line). PMT: photomultiplier; PBS: polarizing beam splitter.

noise at sub-Hz frequencies. The data-taking run consists of recording the demodulated resonance signal in successive 10-min-long time series with 16-bit resolution, at a rate of ≈ 406.5 Sa/s. We alternate acquisition between three modulation frequencies: 873 Hz, 884 Hz and 895 Hz. The total acquisition time is 144 h, corresponding to 864 time series, evenly distributed among the three modulation frequencies.

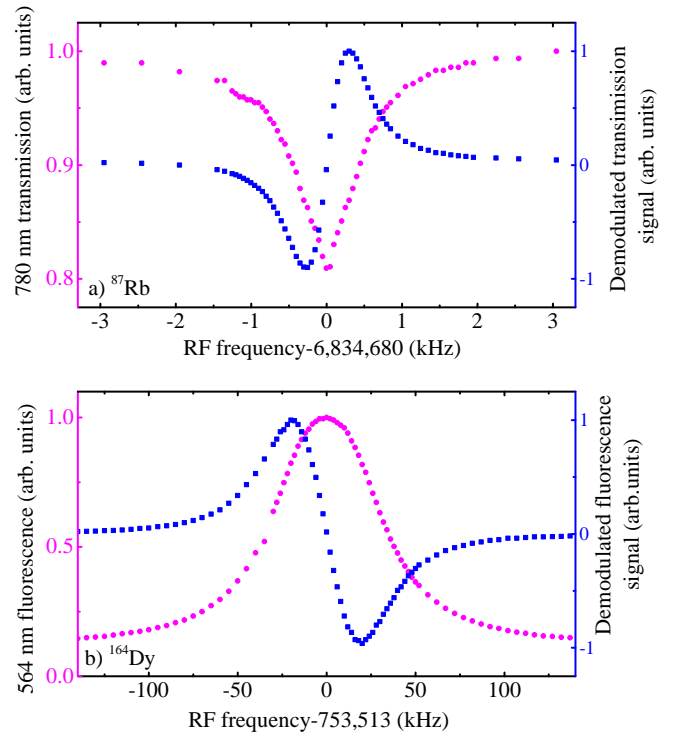


FIG. 7: a) Hyperfine resonance spectrum for ^{87}Rb in the high-frequency run. The blue line shows the rf resonance, and the magenta line indicates the derivative lineshape acquired with the lock-in amplifier. b) rf resonance spectrum for ^{164}Dy . The colors correspond to signals as in a).

Experiment 2 — We acquire data in a run that covers the entire investigated 2.5 mHz–200 Hz frequency range. We record a time series of demodulated rf-resonance signal in successive 4-h-long time series with 16-bit resolution at ≈ 406.5 Sa/s, for a total of 12 h. Each 4-h-long time series is recorded with a dedicated modulation frequency for the rf field: 10,000 Hz, 9,984 Hz or 9,968 Hz.

C. Data analysis

1. Obtaining averaged power spectra

Experiment 1 — The data acquired for the low- and high-frequency ranges of Experiment 1 are analyzed separately.

For the low-frequency range, a Hann window is applied to the 4-h-long time series to avoid unwanted effects in the discrete Fourier Transform (DFT) which is subsequently performed on these data. From the DFT, power spectra of the 4-h-long data are obtained. The power spectra acquired with different modulation frequencies are averaged separately [48]. Therefore, two averaged power spectra are computed, corresponding to the two modulation frequencies used in the low-frequency runs,

as shown in Fig. 8 a.

Complications arise with further averaging of these two power spectra because excess noise power appears in some frequency ranges of the spectra, as shown in the inset of Fig. 8 a. The origin of this excess power is predominantly pickup from laboratory sources, that drifts in frequency, thus appearing as a broad-noise background in the average spectrum. Further combining the two averaged power spectra, would practically result in no improvement in the UBDM detection sensitivity within the region of such a broad excess-power background, as the noise in the resulting spectrum would be almost completely determined by the spectrum having the least noise.

To carry out further analysis of the low-frequency data, we use the following protocol:

1. In frequency windows where no excess power is observed, all power spectra acquired with different modulation frequencies are directly averaged.
2. In frequency windows where broad excess-power background is observed in one of the spectra (at least 40% higher power compared to the vicinity of the window), only the data from the other(s) are retained and further averaged.
3. In the frequency windows where excess power is observed in all spectra, only the data from the spectrum with the least excess power are retained.

With application of this protocol, we arrive at a final averaged power spectrum that is indicated as ‘Combined’ in Fig. 8 a.

Analysis for the high-frequency range of Experiment 1 is done similarly. From the recorded 10-min-long time series, we compute averaged power spectra (Fig. 8 b), that we further combine using the above protocol to arrive at a final power spectrum that is labeled ‘Combined’ in Fig. 8 b.

Experiment 2 — The data analysis for Experiment 2 is more straightforward. This is because broad excess-noise backgrounds that complicate analysis in Experiment 1, are absent here. The three recorded time series (4-h-long each) are computed to obtain respective power spectra, each belonging to one of the three modulation frequencies used in data acquisition. The three power spectra are further averaged together directly, yielding a final power spectrum, which is shown in Fig. 8 c.

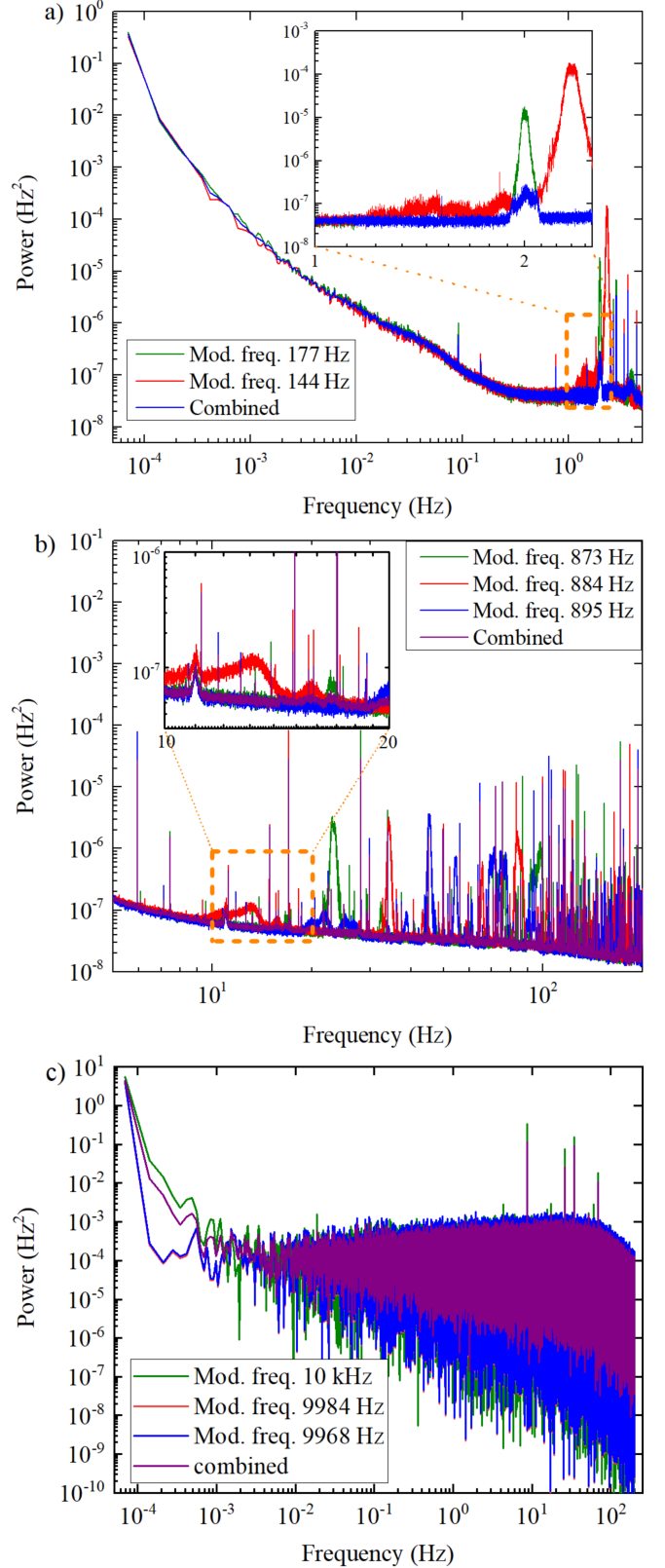


FIG. 8: Averaged power spectra computed from different measurements. a) Low-frequency spectra of Experiment 1. b) High-frequency spectra of Experiment 1. c) Spectra of Experiment 2. See text for details.

2. Obtaining constraints on $\delta f/f$

The procedure to obtain a 95%-confidence-level (C.L.) threshold for detection of oscillations in the spectrum of $\delta f/f$ is the same for Experiment 1 and 2.

An amplitude spectrum is obtained by taking the square root of the final power spectrum obtained as described in Sec. C1. The noise of this spectrum (with the exclusion of frequency bins containing obvious spurious signals) follows a Gaussian distribution, as shown in Fig. 9a. To identify spurious signals within the amplitude spectrum, the amplitude of each frequency bin is compared with the noise in its vicinity.

The standard deviation σ of the noise gives a natural scale to set a threshold to discriminate the spurious signals from the noise background. An example of such a signal, denoted as outlier, is shown in Fig. 9b.

To obtain the σ of the amplitude spectrum, its baseline is first removed. This is done to improve the accuracy in the subsequent calculation of the moving σ of the spectrum, primarily because the varying noise power at low frequencies (the pink or $1/f$ noise) impacts the calculation. To compute this baseline, a moving 50%-percentile filter is applied to the spectrum within a frequency window of 100 bins. (A 50%-percentile filter applied to normally distributed data, provides the mean value of the data set; see Fig. 9a). After subtracting the computed baseline from the spectrum, a moving 50%-percentile filter and a moving 15.9%-percentile filter are applied to the spectrum, using the same window width (i.e. 100 bins). (A 15.9%-percentile filter applied to a set of normally distributed data gives the value that is 1σ below the mean value; see Fig. 9a.) Subtracting the respective filter outputs yields the moving σ of the amplitude spectrum.

However, there are flaws in applying a percentile filter in the low-frequency end of the spectra. First, the application of the filter within a window of N bins, naturally fails for the first $N/2$ bins that need to be discarded. Second, a successive application of the filter to compute the spectrum's σ would force us to discard an additional $N/2$ bins, for a total of N bins. Third, the rapidly varying $1/f$ noise impacts the precision of the calculation.

To compute the spectrum baseline at low frequencies and avoid discarding data points, we instead compute the baseline in the low-end by fitting to the noise (as mentioned, dominated by the $1/f$ contribution). The fit is to the first 200 bins of the spectrum (i.e. the range up to 14 mHz). After the subtraction of this baseline, we then proceed with calculating σ , by applying a moving 50%-percentile filter and a moving 15.9%-percentile filter to the spectrum (within a reduced-size window of 70 bins below 7 mHz), as explained above.

However, it is not possible to reliably calculate the moving σ at the lowest frequencies. Although, in principle, we could probe for oscillations at the lowest frequency $70\ \mu\text{Hz}$ (i.e. the width of a bin), there are two issues: first, the need for sizable width of the window used in the applied percentile filters (windows that are tens

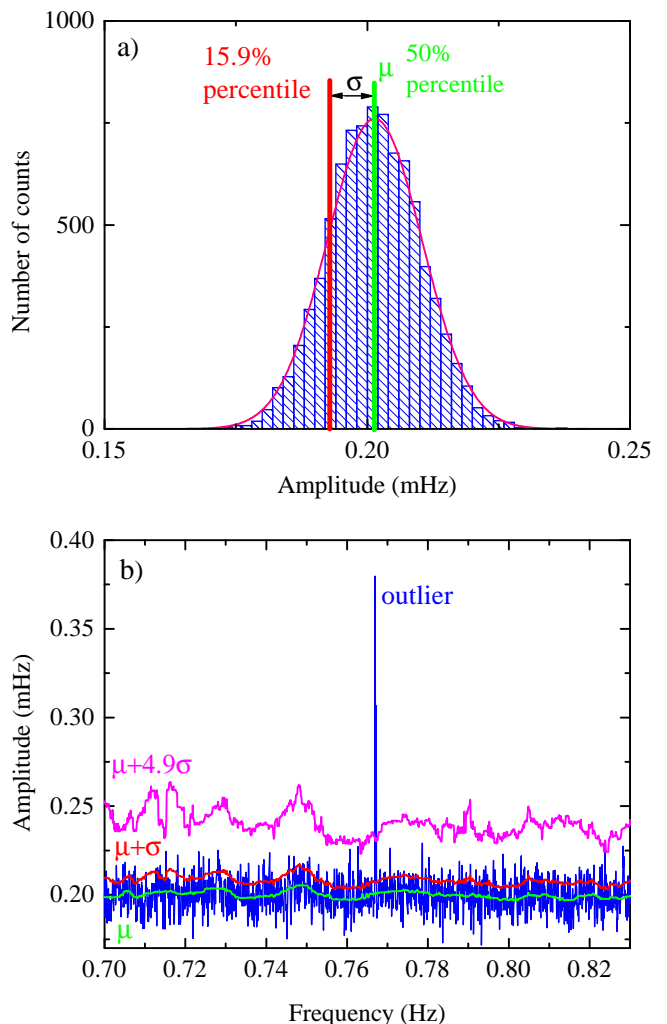


FIG. 9: a) Distribution of noise calculated from data acquired in Experiment 1, in a frequency window 0.5–1.1 Hz. The noise distribution is well approximated with a Gaussian. Here, μ is the median, and σ is the standard deviation. b) An example of a spurious peak observed in the frequency window 0.7–0.83 Hz in Experiment 1, denoted as an outlier.

of bins wide are needed); second (as mentioned above), the increasing $1/f$ noise at low frequencies. Being unable to reliably compute moving σ below 1 mHz, we conservatively employ computed σ for frequencies $f_C \geq 2.5$ mHz.

From the computed σ spectra, a threshold for investigating spurious signals in the $\delta f/f$ spectra is set considering the ‘look-elsewhere’ effect [65], and the respective bin numbers in the spectra of Experiment 1 ($n = 188364$) and Experiment 2 ($n = 2879971$). The computed 95% C.L. thresholds are, respectively, set to 4.9σ and 5.32σ .

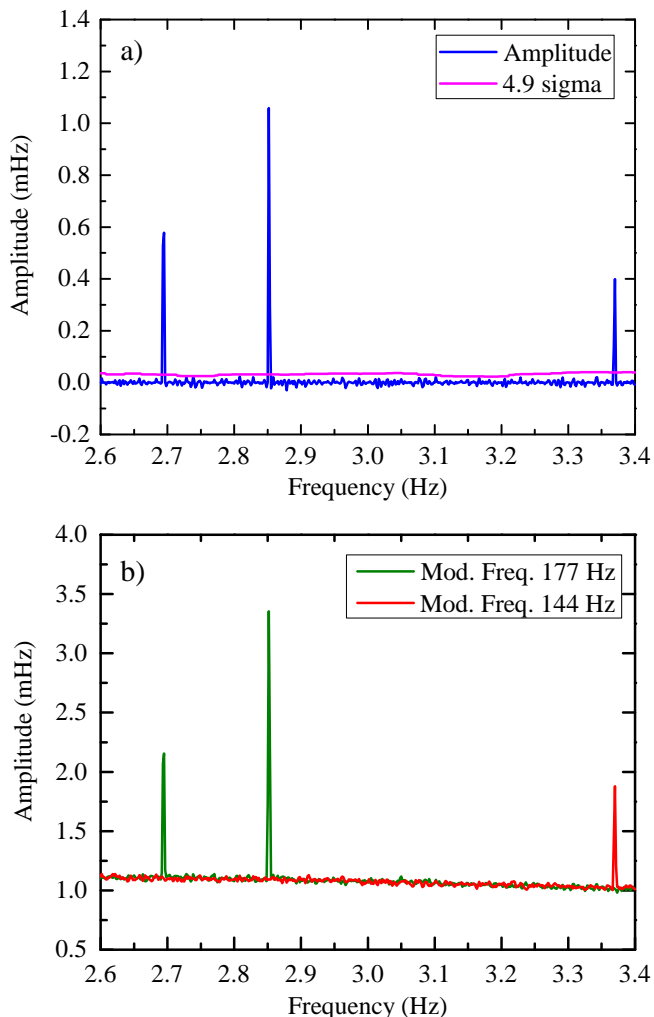


FIG. 10: a) Identification of candidate peaks. Three peaks are shown in the frequency window 2.6–3.4 Hz for the low-frequency measurement in Experiment 1. b)

Intercomparison of spurious peaks in separate amplitude spectra averaged by the data acquired with different modulation frequencies. All the peaks shown here are detected only in one of the spectra for the respective frequency bin and can be eliminated.

3. Investigating spurious signals

Peaks in the obtained amplitude spectra with size exceeding the set threshold are potential UBDM signals (see Fig 10 a). To investigate whether these peaks are real or spurious, various measures were taken, which are discussed separately for Experiments 1 and 2.

Experiment 1— A total of ten candidate peaks were identified in the amplitude spectrum of the low-frequency run of Experiment 1. An example of a strategy to investigate them is shown in Fig. 10. The amplitude spectra separately averaged for the different modulation frequencies are compared, as shown in Fig. 10 b. If the candidate peaks are not observed at the same frequency in all am-

plitude spectra, they can be eliminated directly. In this way, seven out of the ten peaks of the low-frequency run can be excluded from being UBDM candidates. Moreover, in the respective frequency bins of the eliminated peaks, the detection threshold has to be recalculated, because data segments used to obtain the averaged amplitude spectra that include the spurious peaks have to be abandoned. For the remaining three candidate peaks appearing in both averaged amplitude spectra at the same frequency, data from the high-frequency run are utilized additionally for intercomparison.

Investigation of spurious peaks in the amplitude spectrum of the high-frequency run is done similarly. Of the 231 peaks observed, 216 were eliminated via intercomparison among amplitude spectra acquired for the three different modulation frequencies used in the run. To further check the remaining 15 peaks, additional data were taken and compared with the main set, as follows: i) with another (fourth) modulation frequency, resulting in additional elimination of seven peaks; ii) using a different signal generator (see Fig. 5), that cleared out the remaining eight peaks.

Experiment 2—The checks of spurious peaks in experiment 2 are done similarly. A total of 983 peaks are detected in the averaged amplitude spectrum, 467 of which can be eliminated via intercomparison among amplitude spectra acquired for the three modulation frequencies of the run. In addition, 514 peaks are excluded by comparing the main data set with an additional set re-sampled using a fourth modulation frequency. Two peaks remain after this process, that are observed at frequencies 34 Hz and 68 Hz in all amplitude spectra. These are excluded by acquiring additional data sets with a different function generator (see Fig. 6a), as it was done in the high-frequency run of Experiment 1.

D. Calibrations

Atomic calibration — Calibration of the atomic response in Experiment 1 is done for the parameters of the high-frequency experimental run. The rf frequency is tuned on the side of the hyperfine resonance, and frequency modulation with a fixed amplitude is imposed on the rf field applied to the atoms. The amplitude of the induced oscillation in the light transmitted through the Rb vapor (i.e. the probe of the hyperfine resonance) is recorded with varying modulation frequency (Fig. 11 a). A curve fitted to these calibration data is applied to the $\delta f/f$ spectrum of Experiment 1 to account for the slight reduction in the atomic response in the high-frequency end of our 2.5 mHz–200 Hz search for oscillating effects.

In Experiment 2, the response of Dy atoms is considered uniform within the 2.5 mHz–200 Hz investigated range, since the observed 50-kHz linewidth of the Dy transition (of natural linewidth ≈ 20 kHz, that is broadened due to the finite transit time of atoms through the interaction region and due to the power of the applied

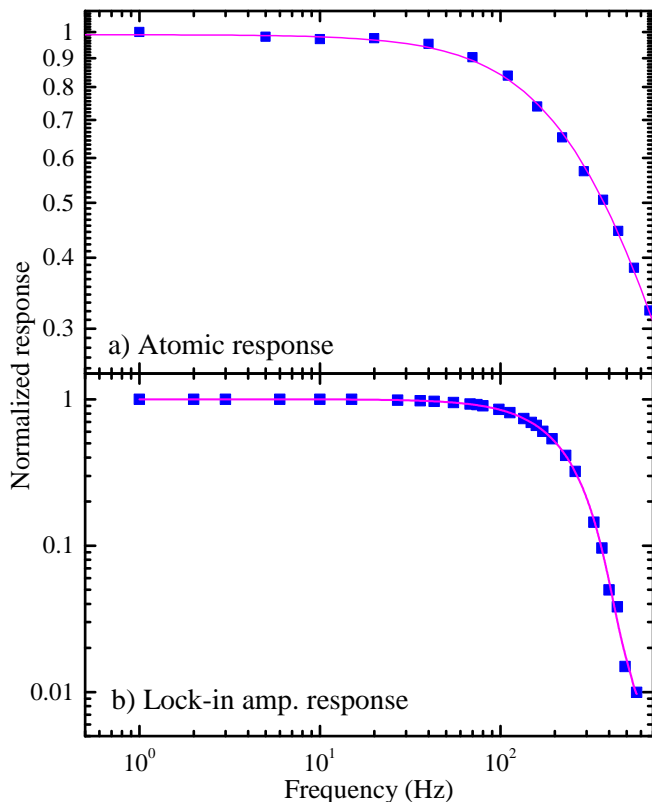


FIG. 11: a) Normalized atomic calibration. b) Normalized lock-in amplifier calibration. The magenta lines represent a fit to measured data points.

rf field) is much greater than the frequencies our search covers.

Lock-in amplifier calibration— Calibration of the lock-in-amplifier response is necessary for both Experiment 1 and 2 to account for low-pass filtering of the amplifier output that becomes significant at the higher frequencies of our search. The calibration is done with the same settings as those in the actual experiments (a 1-ms time constant and a filter slope of 18 dB/octave). A sinusoidal signal with a 10-kHz frequency is measured with the lock-in amplifier. The signal amplitude is modulated slightly at a frequency f_{mod} , causing the amplifier output to oscillate at the same frequency. (This oscillation is the signature expected in the presence of UBDM-induced oscillations, thus the calibration setup emulates the actual experiments.) The amplitude of the lock-in-output oscillation is measured against f_{mod} ; the result is shown in Fig. 11 b. We see that the response is attenuated by $\approx 2\times$ for the highest frequency within our search (200 Hz). We apply corrections to all the UBDM constraints to account for the lock-in-amplifier response.

E. Artificial signal injections

To check the validity of the set 95% C.L. detection thresholds in the $\delta f/f$ spectra, we inject artificial signals of known amplitudes, frequencies and phases to the experimentally obtained time-series data. This is done for 20 frequency values spanning our 2.5 mHz–200 Hz UBDM-search range, and several phase values for each frequency. The amplitudes of these injected signals approximately match the previously set detection thresholds. We find that the signals appear in the resulting $\delta f/f$ spectra with amplitudes ≈ 1.3 times smaller than expected. We multiply the $\delta f/f$ spectra and the obtained detection thresholds by this factor, to re-calibrate apparatus sensitivity. The observed discrepancy is the result of computing the injected-signal amplitudes using amplitude spectra. If one instead uses power spectra, the computed amplitudes are as expected. The discrepancy occurs in the limit of small injected signals (i.e. signals with amplitudes on the order of the noise level). In the limit of large signals (i.e. amplitudes that are at least tens of times greater than the noise level) the obtained amplitudes in the $\delta f/f$ spectra tend to the expected size, thus providing a check for the apparatus calibration.

F. Dependence of m_p and g_{nuc} on the field $\phi(t)$

Let us consider QCD axion models where a pseudo-scalar field, $\phi(t)$, the axion, couples to the gluon field of strength $G^{\mu\nu}$, contributing a term to the Lagrangian density:

$$\mathcal{L} \supset \frac{g_s^2}{32\pi^2} \frac{\phi}{f_\phi} G^{\mu\nu} \tilde{G}_{\mu\nu}, \quad (10)$$

where f_ϕ is the axion decay constant, g_s is the strong coupling constant and $\tilde{G}_{\mu\nu}$ is the dual gluon field strength. We keep the color indices implicit. Considering interactions at energies much lower than the QCD confinement scale, Λ_{QCD} , this term gives rise to coupling of the axion to the hadrons. Specifically, the pion mass depends on the axion field as [56],

$$m_\pi^2(\theta_{\text{eff}}) = \frac{\Lambda_{\text{QCD}}^3}{f_\pi^2} \sqrt{m_u^2 + m_d^2 + 2m_u m_d \cos(\theta_{\text{eff}})}, \quad (11)$$

where we have defined $\theta_{\text{eff}} = \bar{\theta} + \phi/f_\phi$ with $\bar{\theta} = \theta + \arg \det(M)$, θ being the QCD θ angle and M is the quark-mass matrix. The parameters m_u and m_d denote the masses of the up and down quarks, respectively, while $f_\pi \approx 92$ MeV is the pion decay constant. The potential of the axion can be written as $V(\theta_{\text{eff}}) = -m_\pi^2(\theta_{\text{eff}})f_\pi^2$ [87] and is minimized when $\langle \theta_{\text{eff}} \rangle = 0$. From this follows $\langle \phi \rangle / f_\phi \big|_{\text{min}} = -\bar{\theta}$ [88]. Thus, by relaxing to the CP conserving vacuum, the axion solves the strong-CP problem dynamically [14–21]. An axion field coherently oscillating around its minimum may account for DM in

the present universe [11–13] and can be represented as $\theta_{\text{eff}}(t) = (\phi_0/f_\phi) \cos(m_\phi t)$ where ϕ_0 is the field amplitude and m_ϕ is the axion mass.

To see how the QCD axion induces time variation of the FCs at the quadratic order, we expand the pion mass close to the minimum of the QCD axion potential and obtain

$$\frac{\delta m_\pi^2}{m_\pi^2} = \frac{m_\pi^2(\theta_{\text{eff}}) - m_\pi^2(0)}{m_\pi^2(0)} \quad (12)$$

$$\simeq -\frac{m_u m_d \theta_{\text{eff}}^2(t)}{2(m_u + m_d)^2} \simeq -0.11 \frac{\phi(t)^2}{f_\phi^2}, \quad (13)$$

where we used the values of $m_{u,d}$ from [89]. As shown

in [22], time variation of the pion mass leads to time variation of the proton mass, m_p , as

$$\frac{\partial \ln m_p}{\partial \ln m_\pi^2} = 0.06. \quad (14)$$

The nuclear g -factor, g_{nuc} , also depends on the pion mass; for ^{87}Rb we have [22]

$$\frac{\partial \ln g_{\text{nuc}}}{\partial \ln m_\pi^2} = -0.024. \quad (15)$$

From Eqs. (13),(14), and (15) one obtains the dependence of m_p and g_{nuc} on the field $\phi(t)$ shown in Eq. (4) and Eq. (5) of the main text.